中國機械工程學刊第四十五卷第四期第 385~396 頁(民國一百一十三年)
Journal of the Chinese Society of Mechanical Engineers, Vol.45, No.4, pp385~396 (2024)

Mechanical Properties and Microstructural Evolution of GTAW Welded Joints on Additively Manufactured Scalmalloy® and Extruded Aluminium Alloys

Celine Turangi*, Marcel Schaefer*, Junior Nomani*, Florian Häslich**, Tim Pasang***, Shih-Jie Gao**** and Pai-Chen Lin****

Keywords：Scalmalloy, GTAW, welding, microstructure

ABSTRACT

Scalmalloy is an aluminium alloy developed for the additive manufacturing process of Selective Laser Melting. Size limitations often occurring in additive manufacturing due to chamber sizes can be overcome by welding parts together and to existing structures. In this paper, the feasibility of gas tungsten arc welding (GTAW) of Scalmalloy and welding Scalmalloy to extruded aluminium alloys using standard aluminium alloy GTAW parameters were demonstrated, and their resulting microstructures and mechanical properties reported. The welded microstructures showed coarse grains, porosity and other defects assumed to be due to unsuitable welding parameters and composition of materials. Tensile properties were much lower than the base metal values due to defects occurring due to welding. Scanning electron microscopy showed a ductile fracture surface with microvoid coalescence. Hardness testing across the welded samples showed softening of the metal in the Scalmalloy fusion zone and heat affected zones. Therefore, the welding parameters need to be optimized to improve mechanical properties and minimise defects.

Paper Received December, 2023. Revised February, 2024. Accepted February, 2024. Author for Correspondence: C. Turangi.

* *School of Engineering, Computing and Mathematical Sciences, Auckland University of Technology, Auckland, 1010, New Zealand*
***Fraunhofer Institute for Manufacturing Technology and Advanced Materials IFAM, Dresden, Germany Branch Lab Dresden Winterbergstrasse 28, Dresden, 01277, Germany*
****Department of Engineering Design, Manufacturing and Management Systems, Western Michigan University, Kalamazoo MI 4900-5200 USA*
*****Department of Mechanical Engineering, National Chung-Cheng University, Chia-Yi, 62102, Taiwan*

INTRODUCTION

Additive manufacturing (AM) is the method of manufacturing components in a layer-by-layer fashion resulting in weight reduction due to greater design freedom and minimisation of material usage. AM can produce extremely small and geometrically intricate parts with ease. Selective laser melting (SLM) is an AM method using a powder bed of material that is melted and solidified in a layer by layer fashion until a component is formed according to computer model data (DebRoy et al., 2018). However, size limitations in AM prevent large scale parts from being built due to the limited footprint of the build platform or the build chamber. Welding additively manufactured parts to each other and existing structures may resolve this issue (Matilainen, Pekkarinen, & Salminen, 2016). Gas tungsten arc welding (GTAW) is a fusion welding process where two metals are joined by melting exposed surfaces by way of an arc and often used in the automotive, aerospace and sheet metal industries to join various parts together for high joint reliability (Shanavas & Dhas, 2017; Subbaiah, 2019). GTAW is the most commonly used process for ferrous and non-ferrous metals. GTAW of aluminium alloys can be done quickly and in almost any environment whilst also being economical. The quality of welded parts depends highly upon welding parameters such as welding current, filler rod, welding speed and arc voltage (Çetkin, Çelik, & Temiz, 2019; Shanavas & Dhas, 2017). Liu et al. (2012) compared GTAW and GMAW (Mig) welding of a 5083Al workpiece. Findings showed that GTAW welded joints were far superior to those of the GMAW welded joints, having fewer defects and better mechanical properties. The weldability of 5052Al was explored by Shanavas and Dhas (2017), where friction stir welding (FSW) was compared to GTAW welding. Although FSW showed better mechanical properties and fewer defects, it can only be done in specific environments. In contrast, GTAW does show inferior mechanical properties but is far more versatile and easier to perform. G. Xu et al. (2016) completed studies on a new Al-Mg-Mn-Sc-Zr alloy having the following composition: Al-5.8%Mg-0.4%Mn-0.25%Sc-0.10%Zr (wt.%). This alloy was GTAW and FSW welded. Mechanical tests were performed, and the microstructure was also observed. FSW showed better mechanical properties than GTAW welded parts but by a difference of <5% for UTS, YS, and elongation to failure. A significant strengthening effect was observed in the Al-Mg-Mn-Sc-Zr alloy due to the forming of secondary coherent nano-scaled Al3(Sc, Zr) particles during each welding process. Scalmalloy is a novel aluminium alloy belonging to 5xxx Al alloy group and was developed by Airbus Group as the more common Al alloys used in SLM (e.g., AlSi10Mg, AlSi12, and AlSi7Mg0.3 belonging to the 4xxx alloys) showed signs of hot cracking and high reflectivity. Scalmalloy is an Al-Mg-Sc alloy containing Zirconium (Zr) traces and is heat treatable, unlike its 5xxx alloys counterparts. Additions of scandium to aluminium alloys has been explored since the 1970s for casting purposes and has caused a substantial strengthening effect due to a finer equiaxed microstructure with Al_3Sc precipitates being established. Scandium also reduces crack propagation and increases mechanical properties; hence Scalmalloy offers high strength and ductility while exhibiting low anisotropy (A. B. Spierings, Dawson, Heeling, et al., 2017; A. B. Spierings, Dawson, Kern, Palm, & Wegener, 2017). Literature on the welding of additively manufactured parts has somewhat been reported (Aboulkhair et al., 2019). Matilainen et al. (2016) observed the effect of laser welding upon additively manufactured powder bed fusion (PBF) fabricated steel parts. When the energy input of the weld was low, the PBF parts showed severe porosity compared to when the energy input was high; cracking was also apparent, thought to be due to residual stresses. However, the PBF fabricated parts could be welded together and produced high-quality welds. A study by Mäkikangas, Rautio, Mustakangas, and Mäntyjärvi (2019) reported the weldability of the selective laser melted AlSi10Mg alloy using laser welding. Laser welding parameters were selected by visual inspection of preliminary welding experiments with the main aim being to achieve a good overall weld shape. The fusion zone (FZ) showed large pores, the largest of which was 0.7mm in diameter leading to an average tensile strength of 163MPa, almost three times less than its as built tensile strength of 444MPa. However, the shape of the weld was good, with very little weld spattering. Wits and Becker (2015) explored the welding of additively manufactured titanium parts and whether these parts could be laser beam welded with the same weld parameters used for conventionally manufactured titanium parts. Their findings showed that weld parameters could not be transferred from one to another. Higher energy input was necessary to obtain a suitable weld geometry for the additively manufactured titanium sample. Findings showed that welding additively manufactured titanium parts with leakproof and high reliability welded joints is possible, but interconnected porosity may exist in the welded zone.

GTAW welding of Scalmalloy, at present, has little to no published data available. However, Scalmalloy is based upon the cast 5083Al alloy, which shows good weldability (Liu et al., 2012). In addition, SLM is considered a type of welding process and those materials that can be used in SLM are known to have good weldability (Maamoun, Xue, Elbestawi, & Veldhuis, 2018; Olakanmi, Cochrane, & Dalgarno, 2015). Therefore, this work is to determine the feasibility of welding Scalmalloy and 5052Al and 5083Al alloys using similar process parameters as GTAW of conventionally manufactured aluminium parts and examine the microstructural evolution and mechanical properties across the weld.

EXPERIMENTAL PROCEDURE

Test Material and Sample Fabrication

Scalmalloy samples were additively manufactured using Scalmalloy powder with particle sizes between 20µm to 63µm. Scalmalloy composition was 4.55Mg-0.65Mg-0.30Zr-0.51Mn-0.16Si-0.14Fe-0.2Zn-0.01Ti-0.01Cu-0.01V-0.04C(wt%). The energy volume density for the manufacturing of Scalmalloy samples was calculated using Equation 1 (Wong & Hernandez, 2012),

$$E_d = \frac{P}{V_d \cdot D_h \cdot T_1} \quad \text{(I)}$$

where E_d is energy density (J/mm^3), P is laser power (W), D_h is hatch spacing (mm), T_1 is layer thickness (µm) and V_d is scanning speed (mm/s). The selected SLM process parameters (shown in Table 1) were chosen as they yielded samples with relatively high strength and hardness properties. The manufactured Scalmalloy samples (60mm x 27mm x 2mm rectangles) and their build orientation are shown in Fig. 1.

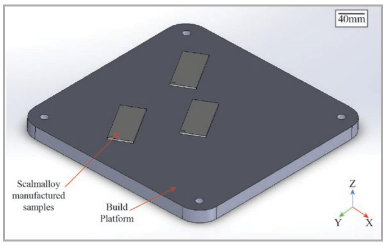

Figure 1 Scalmalloy manufactured samples showing build orientation on platform

The horizontal build (XY) orientation was chosen as it is often used in industrial applications since it has the shortest build time and reduced material usage. Extruded sheets of 5083Al and 5052Al were commercially supplied, wire cut into rectangles 60mm x 27mm in size, and machined to 2mm in thickness.

Table 2 selective laser melting process parameters

Process parameters	Values
Machine	Renishaw AM 400
Laser Power (W)	400
Layer Thickness (µm)	30
Hatch Distance (µm)	150
Scan Speed (mm/s)	1111
Energy Volume Density (J/mm³)	80
Scan Strategy	Bi-directional; Alternating 67º
Laser Focus Diameter (µm)	70

Scalmalloy and aluminium samples were then GTAW welded together using a *Hobart Tigwave 250 AC/DC Arc Welder.* Welding parameters were selected based upon literature (Lei, Deng, Peng, Yin, & Xu, 2013; Liu et al., 2012; Shanavas & Dhas, 2017; G. Xu et al., 2016; P. Xu et al., 2018) and are listed in Table 3. The only varying welding parameter was the welding current due to the differing compositions of each alloy. The welding current of each material is listed in Table 4 and were found through preliminary tests.

Table 3 Gas tungsten arc welding parameters

Parameters	Values
Electrode Material	Tungsten
Welding Angle (º)	≈ 45
Filler Wire	5356Al
Electrode diameter (mm)	2
Weld Speed (mm/s)	3.6
Shielding Gas	Argon
Welding/Gas Flow (l/min)	81
Electric Current Type	AC – High Frequency, Continuous
Welding Voltage (V)	9

Table 4 Selected welding currents for Scalmalloy, 5052Al and 5083Al alloys

Welding Parameters	Values
5083Al Welding Current (A)	85
5052Al Welding Current (A)	88
Scalmalloy Welding Current (A)	81

MECHANICAL TESTING AND ANALYSIS METHODS

An Autograph Universal Testing Machine Ag-Is (Shimadzu, Kyoto, Japan) with a crosshead speed of 0.07 mm/s was used. Three samples were tensile tested for each condition including the base metal substrates. Following welding, tensile samples were wire cut to the geometry shown in 2a. It should be noted that tensile samples were tested in the as welded (AW) condition, where the weld bead remained intact, and post-machined (PM) condition, where the weld bead had been wire cut (machined) to suit the overall sample thickness of 2mm. The PM samples ensure that the area for tensile testing was uniform and tensile results were not influenced by a variable cross section by the weld bead remaining intact. AW samples were included for information since it is not always possible or practical to remove the weld bead in real life applications. The tensile strengths of each sample were calculated individually using their nominal cross sections given in Fig 2. PM samples had a nominal cross section of 6mm and 2mm (Fig. 2c) to suit the overall uniform thickness of the sample. The AW samples had a nominal cross section of 6mm and 4mm due to the size of the weld bead (Fig. 2d). The approximate proportions for base metal substrates to welded zone is given in Fig. 1d for information as the elongation will be measured along the overall length of the sample. Note also that the welded region is always located in the centre of the tensile specimen. A *Hitachi SU-70 Schottky* field emission scanning electron microscope (SEM) was used for fracture analysis of samples. All test samples were then metallographically prepared by cutting, mounting, grinding, and polishing. The cross-sectioned surface of the mounted samples was then etched using Keller's reagent, a solution of 2.5% HNO3, 1.5% HCl, 1% HF and the balance was distilled water, to reveal the microstructure. The microstructure, including defects, of the welded joints were then observed using an *Olympus BX51M* Optical Microscope and SEM.

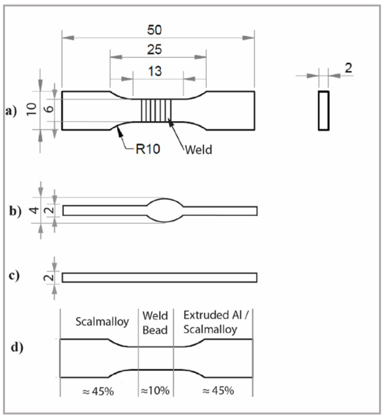

Fig. 2 Geometry of tensile test specimen showing

dimensions. Side view of b) as welded cross-sectional view and c) post machined cross-sectional view and d) the approximate proportions of Scalmalloy, extruded Al alloy and welded metal over the entire length of the sample. Units are in mm.Lastly, Vickers microhardness was performed on each metallographically prepared sample using an *LM800AT tester* with a dwell time of 10 seconds and a load of 100fg. Five rows of twenty-two indentations were placed 1mm apart to map the hardness profile across the weld for each welded condition starting from Scalmalloy base metal to the end of each welded cross section. The average hardness value was plotted.

RESULTS

Microstructure

Fig. 3a shows the macrostructure of the Scalmalloy welded joint, Fig. 4a shows the macrostructure of Scalmalloy-5052Al welded joint, and Fig. 5a shows the macrostructure of Scalmalloy-5083Al welded joint. The base metal (BM), fusion zone (FZ) and heat-affected zone (HAZ) are identified in these figures. The overall weld shape for each welded joint is uniform, however defects, such as pores 1µm to 200µm in size, can be seen in the FZ of all samples. The HAZ regions for the Scalmalloy welded joint and the Scalmalloy sides of the extruded aluminium alloy joints exhibited many large pores compared to the HAZ region on the extruded aluminium alloy sides that exhibited no defects at all. The porosity seen primarily in the HAZ and FZ of the Scalmalloy welded joint and the HAZ Scalmalloy sides of the extruded aluminium alloy joints (Fig. 3, 4 and 5) was assumed to be predominantly due to the formation of hydrogen pores as it is reported that hydrogen can be introduced into the Scalmalloy metal powder from the environment by air or humidity. This hydrogen is then trapped during the SLM process and remains in a metastable state within the material. This trapped hydrogen reintegrates into the material via the high heat introduced during the welding process causing a large and sudden rise in the volume of gas (mainly hydrogen) leading to the formation and presence of pores in the welded metal. It's also clear that the aluminium oxide that is evenly distributed in the SLM process and is present in most SLM manufactured parts give rise to the generation of these pores (Michler, Hollmann, Zenker, & Buchwalder, 2021; Weingarten et al., 2015). Porosity is much lower in the extruded aluminium and Scalmalloy welded joints as the welding parameters are much more suited to the extruded aluminium alloys (Shanavas & Dhas, 2017; Wits & Becker, 2015). Fig. 3e shows the microstructure of the Scalmalloy BM. It is characterised by layered molten pool tracks where the molten pool size is approximately 100 to 200µm in size. This layered Scalmalloy BM microstructure is the result of the layer-by-layer SLM manufacturing process (Jannet, Mathews, & Raja, 2014; A. B. Spierings, Dawson, Heeling, et al., 2017; Ye et al., 2017). Very fine grains and fine second phase particles of $Al_3(Sc, Zr)$ have been reported to reside in the Scalmalloy BM microstructure pinning grain boundaries, which increase the overall strength of Scalmalloy (Huang, He, Wang, & Tang, 2019; A. B. Spierings, Dawson, Heeling, et al., 2017; Adriaan B. Spierings, Dawson, Voegtlin, Palm, & Uggowitzer, 2016).

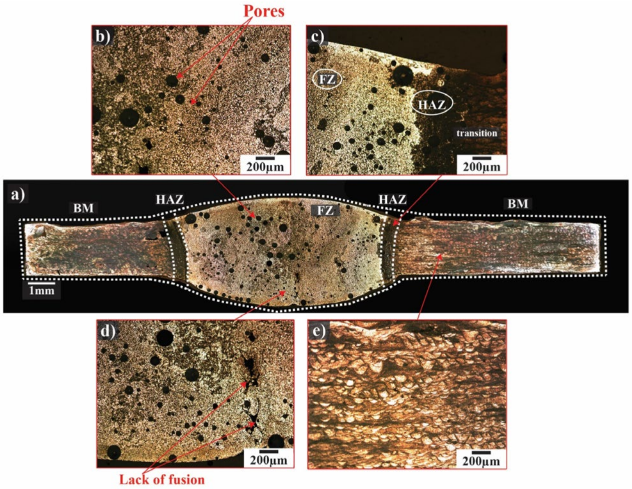

Fig. 3 Scalmalloy welded joint - a) overall macrostructure of welded joint, b) fusion zone with pores, c) heat affected zone with pores, d) fusion zone showing lack of fusion on bottom of weld, e) Scalmalloy base metal

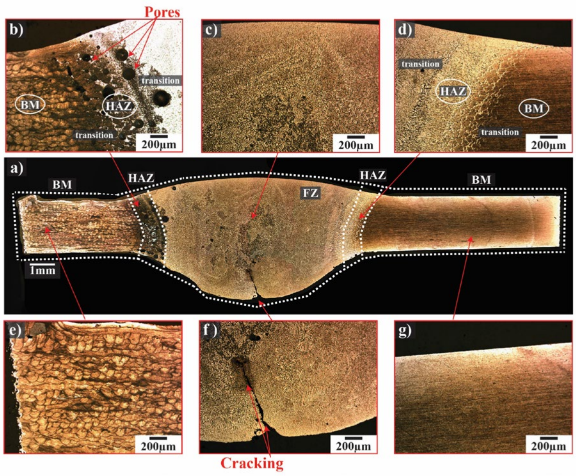

Fig. 4 Scalmalloy-5052Al welded joint - a) overall macrostructure of welded joint, b) heat affected zone of Scalmalloy side, c) fusion zone, d) heat affected zone of 5052Al side, e) Scalmalloy base metal, f) fusion zone, g) 5052Al base metal

The same layered Scalmalloy BM structure is also seen in Fig. 4e and Fig. 5e of the Scalmalloy-5052Al welded joint and the Scalmalloy-5083Al welded joint, respectively. Fig 4g and 5g show the base metal microstructures of the 5052Al and 5083Al alloys, where higher magnification of these areas are seen in the SEM micrograph shown in Fig. 6b. The microstructure of the extruded aluminum alloys is characterised by elongated grains running parallel along the direction of extrusion which is consistent with the typical microstructure of both 5052Al, 5083Al and other extruded aluminium alloys. Al_6Mn phase dissolution is also apparent from the visible voids, which is an artifact of the etchant due to the magnesium content.

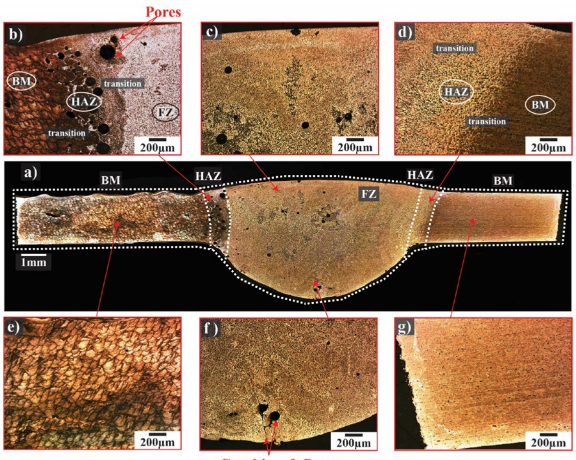

Fig. 5 Scalmalloy-5083Al welded joint - a)) overall macrostructure of welded joint, b) heat affected zone on Scalmalloy side, c) fusion zone, d) heat affected zone on 5083Al side, e) Scalmalloy base metal, f) fusion zone, g) 5083Al Scalmalloy base metal

Fig 3c, Fig. 4b and Fig. 5b show the HAZ of the Scalmalloy side for the Scalmalloy, Scalmalloy-5052Al and Scalmalloy-5083Al welded joint, respectively. Additionally, Fig. 7a - 7c show high magnification SEM micrographs of these areas, which are characterised by the molten pool tracks on Scalmalloy BM side transitioning into coarsened columnar grains with large hydrogen induced pores, approximately 100µm in size (Schwarz, Schleser, Gerhardts, Popoola, & Gebhardt, 2021). Fig. 4d and Fig. 5d show the HAZ of the extruded aluminum alloys sides of the welded joints for Scalmalloy-5052Al and Scalmalloy-5083Al, respectively. These exhibit similar characteristics to each other and to the HAZ on the Scalmalloy sides with columnar grains transitioning into equiaxed grains and leading into fine recrystallised grains in the FZ, but with almost no porosity or other visible defects due to welding parameters being more suited to the extruded aluminium alloys. These columnar grains then transition into equiaxed grains leading into the FZ. The structure of the HAZ for both Scalmalloy and the extruded aluminium alloys is due to the high welding heat that has caused the coarsening of grains to occur and then to eventually recrystallise in the FZ (Guo, Pan, Ren, & Quan, 2018; Hakem, Lebaili, Miroud, Bentaleb, & Toukali, 2012; Shanavas & Dhas, 2017; G. Xu et al., 2016; P. Xu et al., 2018).

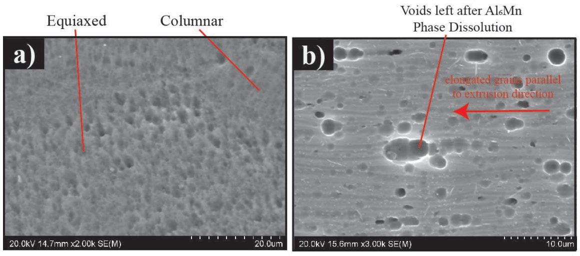

Fig. 6 SEM micrograph of a) Scalmalloy base metal and the b) extruded Al alloy base metals

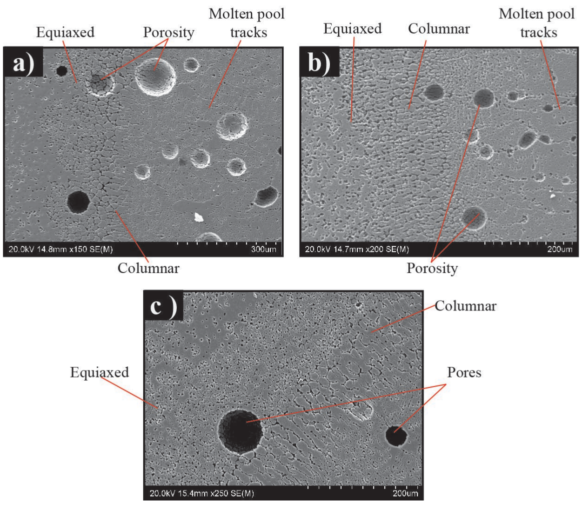

Fig. 7 SEM micrograph of heat affected zone Scalmalloy side - a) Scalmalloy welded joint, b) Scalmalloy-5052Al welded joint, c) Scalmalloy-5083Al

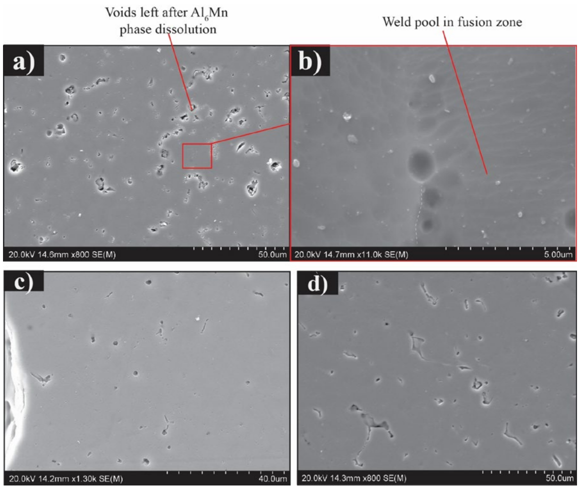

Fig. 8 SEM micrograph of fusion zone welded joints -a) Scalmalloy welded joint fusion zone, b) magnified image of Scalmalloy-Scalmalloy fusion zone, c) Scalmalloy-5052Al fusion zone, d) Scalmalloy-5083Al fusion zone

Fig 3b and Fig 3d show the microstructure of the FZ of the Scalmalloy welded joint. Pores 5µm to 200µm in size, can be seen in Fig 3b, while Fig. 3d shows pores and lack of fusion occurring at the bottom of the weld centre. Fig. 4c and Fig. 4f show the FZ of the Scalmalloy-5052Al welded joint and Fig. 5c and Fig. 5f show the FZ of the Scalmalloy-5083Al welded joint. These exhibit similar microstructure to the FZ of the Scalmalloy welded joint, but with much less porosity and smaller pore sizes of 10µm to 50µm. Fig. 4f and Fig. 5f show the bottom half of the FZ for the Scalmalloy-5052Al and Scalmalloy-5083Al welded joints, respectively. Cracking and lack of fusion has occurred here in the weld centre thought to be due to low power delivery to the weld and too large a weld pool (Çetkin et al., 2019). High magnification SEM micrographs of the FZ of each joint is shown in Fig. 8a – 8d for the Scalmalloy, Scalmalloy-5052Al and the Scalmalloy-5083Al welded joints, respectively. The FZ of each welded joint exhibit very similar characteristics such as fine recrystallised grains with small voids due to Al_6Mn phase dissolution (Hakem et al., 2012). Fig. 8b shows a magnified area of Fig. 8a with visible GTAW weld pool tracks. Table 5-7 shows the composition of the HAZs and FZs for the Scalmalloy, Scalmalloy-5052Al and Scalmalloy-5083Al welded joints, respectively. T There is no significant change in either of the FZ for each welded joint where, very high aluminium and median magnesium content were detected. There is little to no detection of scandium, zirconium, and manganese in the FZ as the temperatures was assumed to be higher than 550°C, as reported in the literature, where $Al_3(Sc, Zr)$ particles that could be present from the Scalmalloy BM would have lost coherency and dissolved. Manganese from the Al_6Mn phase would also be detected here as this is a typical phase which develops in aluminium alloys with magnesium content between 3% to 5% upon solidification, however it has been dissolved by the etchant, Keller's Reagent (Algendy, Liu, & Chen, 2020). Hence, a supersaturated aluminium solid solution has formed here with fine recrystallised grains induced by the high heat of GTAW like that seen in G. Xu et al. (2016), Lei et al. (2013) and Arunkumar and Subbaiah (2019).

Furthermore, a line scan detecting elements of scandium and zirconium is shown in Fig. 9 for the Scalmalloy welded joint. As the line scan moves through the HAZ to the FZ, scandium and zirconium elements are more prominent in the HAZ as the temperatures here are assumed to reach up to 500°C, hence, $Al_3(Sc, Zr)$ particles that could be present still remain coherent with the matrix. Scandium and zirconium become less obvious through the FZ due to these elements dissolving under the high heat caused by GTAW. There is also some scandium and zirconium build up at the transition from HAZ to FZ, showing the clear separation of zones by the elements detected in these regions G. Xu et al. (2016).

Table 5. Energy dispersive spectroscopy scan results of the heat affected zone and the fusion zone of the Scalmalloy welded joint Scalmalloy welded joint

Welded joint/Element	Mg	Al	Sc	Mn
Scalmalloy-Scalmalloy HAZ	3.03	95.63	0.69	0.65
Scalmalloy-Scalmalloy FZ	4.50	95.03	0.14	0.34

Table 6. Energy dispersive spectroscopy scan results of the Scalmalloy heat affected zone fusion zone of the Scalmalloy-5052Al welded joint

Welded joint/Element	Mg	Al	Sc	Mn
Scalmalloy-5052Al FZ	3.34	96.35	0.13	0.19
Scalmalloy-5052Al HAZ	2.93	95.89	0.54	0.64
Scalmalloy-5052Al FZ	2.98	96.47	0.22	0.34

Table 7. Energy dispersive spectroscopy scan results of the heat affected zone and the fusion zone of the Scalmalloy-5083Al welded joint

Welded joint/Element	Mg	Al	Sc	Mn
Scalmalloy-5083Al FZ	4.10	95.28	0.22	0.4
Scalmalloy-5083Al FZ pt1	4.64	94.90	0.14	0.32
Scalmalloy-5083Al FZ pt2	8.28	90.89	0.18	0.29
Scalmalloy-5083Al FZ pt3	5.01	94.46	0.22	0.32
Scalmalloy-5083Al FZ p4	4.36	92.37	0.12	3.14

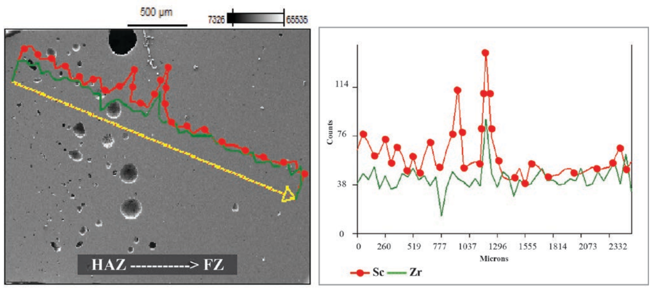

Fig. 9 Line scan detecting elements of scandium and zirconium from heat affected zone to the fusion zone of the Scalmalloy welded joint

Microhardness

Microhardness distributions perpendicular to weld direction are shown in Fig. 10. The yellow dashed line in these figures indicate the average hardness of the base metal of Scalmalloy as a reference line. In Fig. 10a for the Scalmalloy welded joint, the lowest microhardness value with an average of 77HV are detected in the FZ, a significant decrease of approximately 40%. As the distance away from the weld centre of the FZ increases, microhardness increases gradually until it passes the HAZ and resumes to the original average hardness of 129HV for Scalmalloy BM. Similarly, Fig. 10b for the Scalmlloy-5052Al welded joint follows the same

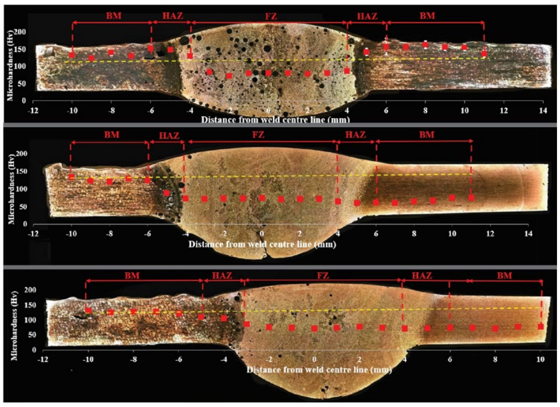

Fig. 10 Microhardness distribution of the all welded joints – a) Scalmalloy-Scalmalloy, b) Scalmalloy-5052Al, c) Scalmalloy-5083Al welded joint

pattern as the previous sample with the lowest average value of 68HV recorded in the FZ dropping from an average of 128HV of Scalmalloy BM. This microhardness value in the FZ remains consistent as it continues through the HAZ to the BM of 5052Al where its microhardness also averages to 68HV. In Fig. 10c, Scalmalloy-5083Al welded joint resembles the same microhardness pattern as Scalmalloy-5052Al, with a sharp drop from the average microhardness measure of 123HV for Scalmalloy BM to an average hardness of 69HV and then remaining consistent through to the 5083Al BM.

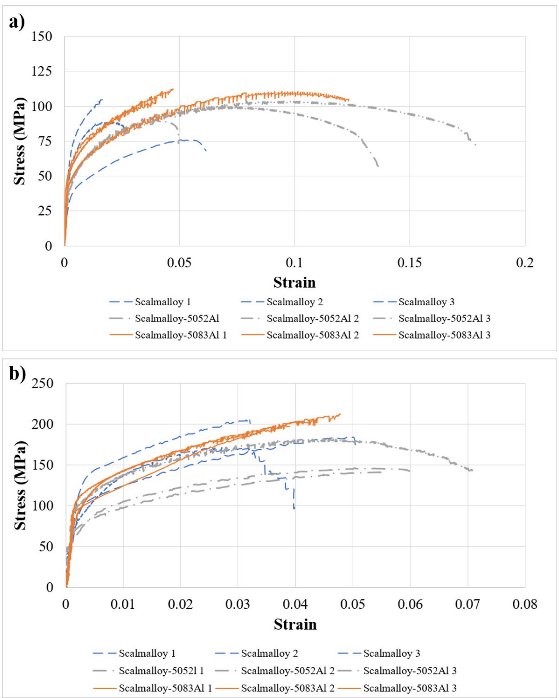

Fig. 11 Stress-strain curves of welded samples – a) As welded condition, b) Post machined condition.

Tensile Properties

Stress strain curves for the AW samples are shown in Fig. 11a and PM samples are shown in Fig. 11b. The AW samples generally had a greater elongation than PM samples, but experienced yield very early and lower ultimate tensile strengths (UTS). However, PM samples have a lower elongation, yet possessed increased yield strengths (YS) and UTS values. Fig. 12 and 13 shows the average YS, UTS and elongation of each welded joint where most samples fractured in the HAZ, except for one sample for each condition that failed in the FZ. Note that Table 8 summarises all tensile data.

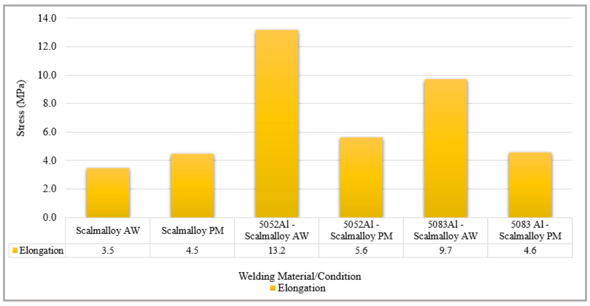

Fig. 12 Average elongation of all each welded condition

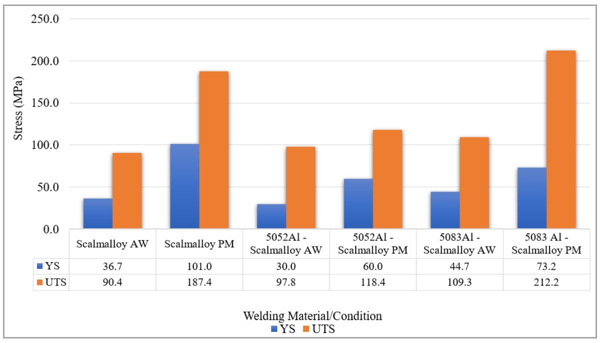

Fig. 13 Average Yield strength and Ultimate tensile strength of all each welded condition

Table 8. Tensile Data Values

Sample condition	**YS (MPa)**	**UTS (MPa)**	**Elongation (%)**
Scalmalloy - Scalmalloy (AW)	37	91	3.5
Scalmalloy - Scalmalloy (PM)	101	188	4.5
Scalmalloy – 5052Al (AW)	30	98	13.0
Scalmalloy – 5052Al (PM)	60	119	5.6
Scalmalloy – 5083Al (AW)	45	110	9.8
Scalmalloy – 5083Al (PM)	74	212	4.6
Scalmalloy BM	288	335	9.8
5052Al BM	161	229	29.0
5083Al BM	232	329	18.0

Fracture Analysis

In Fig. 14 and Fig. 16, all samples had a reasonably flat fracture surface where the majority had fractured in the HAZ on the Scalmalloy sides. Micro voids, extensive porosity and dimples are evenly distributed on the samples that fractured on the Scalmalloy side for the Scalmalloy and Scalmalloy-5083Al welded joints. Some large spherical gas pores can be observed on the fracture surfaces in Fig.14b and 14f along with some incomplete melting and lack of fusion developed during the SLM process and is similar to the Scalmalloy-5083Al sample shown in Fig 16b and Fig. 16f. In Fig. 15, the Scalmalloy-5052Al samples had a more deformed fracture surface than the other two samples as it fractured on the 5052Al alloy side, rather than the Scalmalloy side.

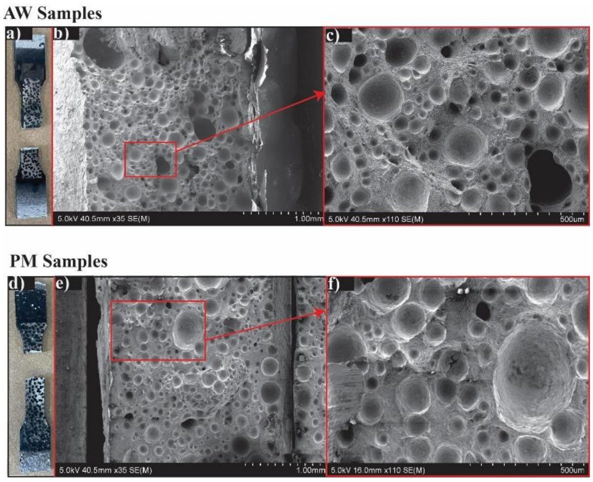

Fig. 14 SEM micrographs of the fracture surfaces of Scalmalloy-Scalmalloy welded samples b), c), e,) f). Macrograph of a side view of fractured samples a), d) – post machined and as welded states are as indicated in the image

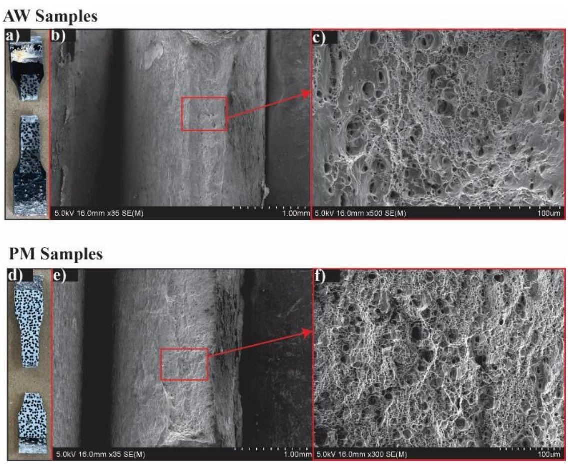

Fig. 15 SEM micrographs of the fracture surfaces of Scalmalloy-5052Al welded samples b), c), e,) f). Macrograph of a side view of fractured samples a), d) – post machined and as welded states are as indicated in the image

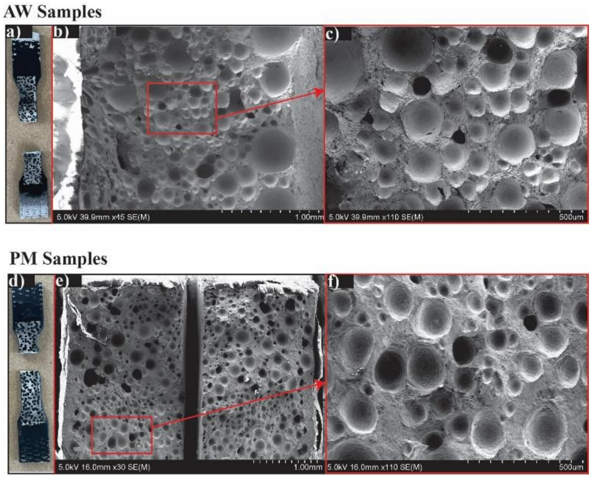

Fig. 16 SEM micrographs of the fracture surfaces of Scalmalloy-5083Al welded samples b), c), e,) f). Macrograph of a side view of fractured samples a), d) – post machined and as welded states are as indicated in the image

DISCUSSION

Effect of microstructure on hardness properties of the welded joints

In welding, excessive heat often leads to coarsening of grains and dislocation movement. However, Scalmalloy is reported to have Al_3(Sc, Zr) particles that are highly coherent with the Al matrix and have good thermal stability. Hence, sub grain and grain boundaries require a large amount of energy to interrupt this coherency. Thus, strengthening by these particles is reported by (Davydov, Rostova, Zakharov, Filatov, & Yelagin, 2000; Jostein Røyset & N. Ryum, 2005; A. B. Spierings, Dawson, Heeling, et al., 2017). The FZ of all samples consisted primarily of an aluminium solid solution induced by the high temperature and heat input from GTAW as well as the addition of the filler wire of 5356Al. As the FZ during GTAW can reach up to temperatures of 600ºC, Al_3(Sc, Zr) particles are reported to become incoherent with the aluminium matrix and scandium and zirconium elements almost completely dissolve when temperatures rise to 550ºC. Hence, it is assumed that strengthening imposed by Al_3(Sc, Zr) particles is lost, and only solution strengthening remains (Arunkumar & Subbaiah, 2019; Lei et al., 2013; Subbaiah, 2019; G. Xu et al., 2016). Additionally, the filler rod material of 5356Al may not be a suitable material for welding Scalmalloy as their compositions differ from one another, leading to lowered hardness in the FZ due to favouring the primary elements of magnesium in the filler rod and extruded aluminium alloys. HAZ of Scalmalloy is affected by welding heat as this causes grain growth; however grain boundaries and pinning of dislocations are reported to remain in this area as the welding temperature is equal to or below 500ºC, and $Al_3(Sc, Zr)$ particles continue to be coherent (Lei et al., 2013; G. Xu et al., 2016). This is demonstrated by the steady regaining of hardness through the Scalmalloy HAZ as the distance away from the FZ increases and eventually reconstitutes through Orowan strengthening from small second phase particles present in the Scalmalloy BM (Davydov et al., 2000; Jostein Røyset & Nils Ryum, 2005). For the Scalmalloy samples welded to both 5052Al and 5083Al, hardness remains at the same level of Scalmalloy BM hardness and drops down through the HAZ and FZ to the average (typical) BM hardness of 5052Al and 5083Al as the welding parameters are suited to these extruded aluminium alloys than for Scalmalloy, as is the filler wire material (Huang et al., 2019; P. Xu et al., 2018; Zazi, Ifires, Mehala, & Chopart, 2017).

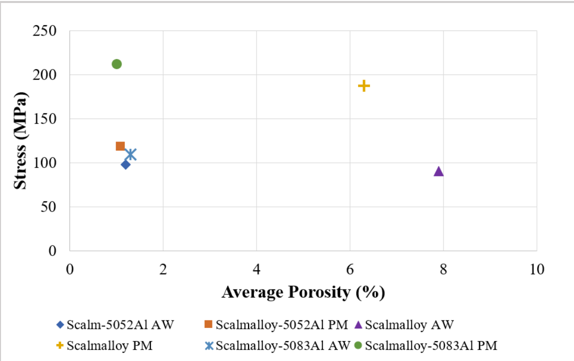

Fig. 17 Comparison of ultimate tensile strengths against the porosity percentage within each welded joint

Effect of microstructure on the tensile properties of the welded joints

The Scalmalloy-5083Al welded joint displayed the highest tensile strength as Scalmalloy and 5083Al BM have similar tensile strengths, and the percentage of porosity present in this sample was much lower than the Scalmalloy welded joint. Scalmalloy welded joint showed the next highest tensile strength as it was assumed that the $Al_3(Sc, Zr)$ particles were still able to pin grain boundaries in the HAZ since welding temperature was not assumed to exceed 500ºC. Scalmalloy-5052Al welded joint had the lowest tensile strength as 5052Al BM has the lowest tensile strength when compared to Scalmalloy and 5083Al BM which is common for this alloy as it is a part of the low to medium strength aluminium alloys (Shanavas & Dhas, 2017; Wang, Chen, Pan, Mao, & Fang, 2015).The AW samples contained the weld bead which acted as a surface defect and exhibited stress concentrations leading to non-uniform load distribution. Fig 17 shows that the AW samples contained a higher percentage of porosity than PM samples as the AW samples had a larger cross-sectional area. The lack of fusion and cracking at the bottom of the weld bead for some of the welded joints can also cause local stress concentration. Consequently, these factors have led to lowered tensile strength in the AW samples. For the Scalmalloy-5083Al welded joint, failure occurred in the HAZ on the Scalmalloy side due to coarse grains and visible porosity. Scalmalloy and 5083Al also have similar tensile strengths. Hence, failure was likely to occur where more visible defects were present. Scalmalloy-5052Al welded joint fractured on the 5052Al HAZ side as this zone exhibited coarse columnar and equiaxed grains and the tensile strength of 5052Al is much lower than that of Scalmalloy.The PM samples all exhibited similar elongation when compared to each other. Again, the porosity and defects developed in the FZ and HAZ would have caused the low elongations especially when compared to the elongations of their respective BM substrates. The UTS, YS and elongation values of the welded joints in both conditions are almost 50% lower than their respective BM substrates. This is mainly due to the interconnected porosity and high porosity percentage in the welded zones and HAZs. The other defects such as cracking and lack of fusion seen in the welded zone have also contributed to the lower tensile properties (Lei et al., 2013; G. Xu et al., 2016).

Determining fracture mechanism for welded joints

All samples fractured in the HAZ due to the prevalent microstructures observed in these areas and the softening of metal occurring due to this region being exposed to the high welding heat. In addition, stress concentrations originating from the cross-sectional changes in the AW samples increased the likelihood of fracture occurring in the HAZ. For the Scalmalloy-5083Al welded joint, failure occurred in the HAZ on the Scalmalloy side due to coarse grains and visible porosity. Scalmalloy and 5083Al also have similar tensile strengths. Hence, failure was likely to occur where more visible defects were present. Scalmalloy-5052Al welded joint fractured on the 5052Al HAZ side as this zone exhibited coarse columnar and equiaxed grains and the tensile strength of 5052Al is much lower than that of Scalmalloy.

The fracture mechanism of the Scalmalloy and Scalmalloy-5083Al welded joints was microvoid coalescence as there are numerous and evenly distributed voids apparent in Fig. 14 and 16 showing ductile behaviour. By observing the shape of the pores visible in Fig. 14 and 16, it can be deduced that these are large gas pores caused by gas entrapment around the melt pool, incomplete melting and solidification due to insufficient energy input during the SLM process (Aboulkhair et al., 2019; Galy, Le Guen, Lacoste, & Arvieu, 2018; Olakanmi et al., 2015; Zhang, Li, & Bai, 2017). Gas porosity and lack of fusion are the most common defects during the

SLM process and some microporosity is typical of AM components. These SLM manufactured samples are prone to melt pool instability and sensitive to unsuitable parameters. The large gas pores shown in Fig. 16c and Fig. 16f are likely due to gas entrapment in the melt pool (Aboulkhair et al., 2019; DebRoy et al., 2018; Galy et al., 2018). The Scalmalloy-5052Al sample shown in Fig. 15 had evenly distributed dimples throughout the fracture surface and evident necking, indicating very ductile behaviour. This is typical for the extruded aluminium alloys as they are of low to medium strength and commonly very ductile consistent with its high elongation listed in Table 8 (Santos Junior, Machado, Falco Sales, Barrozo, & Ezugwu, 2016).

CONCLUSION

GTAW samples of the additively manufactured, Scalmalloy, and extruded aluminium alloys, 5052Al and 5083Al, were investigated in the as welded (AW) and post machined (PM) conditions. The mechanical properties and microstructure of the welded samples were analysed by microhardness tests, tensile tests, and microscopy. The results of this work are listed in the following:

1. An aluminium solid solution with very fine recrystallised grains was formed in the FZ of each welded joint assumed to be due to the high heat from GTAW and composition of substrates. The Scalmalloy HAZ consisted of many defects and coarsened grains, while extruded aluminium alloy HAZ sides contained almost no porosity as welding parameters were more suited to the extruded aluminium alloys than Scalmalloy.
2. Microhardness across the weld was consistent with softening due to the high heat of welding and consistent with the compositions of the materials.
3. Tensile properties for the welded joints were much lower than their respective BM substrates due to interconnected porosity and defects in the welded regions.
4. A ductile fracture mechanism was visible on all conditions due to the many dimples present on the surface.

Based upon the above results, it is feasible to weld Scalmalloy using GTAW and feasible to weld Scalmalloy to extruded aluminium alloys using standard GTAW parameters for extruded aluminium alloys. However, these welds fractured in the HAZ and FZ of the samples, as a result of much lower UTS and YS values than their BM substrates. This indicates that the standard GTAW parameters for extruded aluminium alloys cannot be simply transferred from conventionally manufactured aluminium alloys to weld Scalmalloy, but rather need to be optimised to improve the mechanical properties and minimise defects within the welded joints observed in this work.

REFERENCES

Aboulkhair, N. T., Simonelli, M., Parry, L., Ashcroft, I., Tuck, C., & Hague, R. (2019). 3D printing of Aluminium alloys: Additive Manufacturing of Aluminium alloys using selective laser melting. *Progress in Materials Science, 106*, 100578. doi:https://doi.org/10.1016/j.pmatsci.2019.100578

Algendy, A. Y., Liu, K., & Chen, X. (2020). *Formation of intermetallic phases during solidification in Al-Mg-Mn 5xxx alloys with various Mg levels.* Paper presented at the MATEC Web of Conferences.

Arunkumar, D., & Subbaiah, K. (2019, 2019). *Effect of Continuous and Pulsed Current Tungsten Inert Gas Welding of Cast Al–Mg–Sc Alloy.* Paper presented at the Advances in Manufacturing Processes, Singapore.

Çetkin, E., Çelik, Y. H., & Temiz, Ş. (2019). Effect of welding parameters on microstructure and mechanical properties of AA7075/AA5182 alloys joined by TIG and MIG welding methods. *Journal of the Brazilian Society of Mechanical Sciences and Engineering, 42*(1), 34. doi:10.1007/s40430-019-2119-7

Davydov, V. G., Rostova, T. D., Zakharov, V. V., Filatov, Y. A., & Yelagin, V. I. (2000). Scientific principles of making an alloying addition of scandium to aluminium alloys. *Materials Science and Engineering: A, 280*(1), 30-36. doi:https://doi.org/10.1016/S0921-5093(99)00652-8

DebRoy, T., Wei, H. L., Zuback, J. S., Mukherjee, T., Elmer, J. W., Milewski, J. O., . . . Zhang, W. (2018). Additive manufacturing of metallic components – Process, structure and properties. *Progress in Materials Science, 92*, 112-224. doi:10.1016/j.pmatsci.2017.10.001

Galy, C., Le Guen, E., Lacoste, E., & Arvieu, C. (2018). Main defects observed in aluminum alloy parts produced by SLM: From causes to consequences. *Additive Manufacturing, 22*, 165-175. doi:10.1016/j.addma.2018.05.005

Guo, Y., Pan, H., Ren, L., & Quan, G. (2018). An investigation on plasma-MIG hybrid welding of 5083 aluminum alloy. *The International Journal of Advanced Manufacturing Technology, 98*(5-8), 1433-1440. doi:10.1007/s00170-018-2206-4

Hakem, M., Lebaili, S., Miroud, J., Bentaleb, A., & Toukali, S. (2012). Welding and characterization of 5083 aluminum alloy. *Metallofizika, 5*, 23-25.

Huang, Q., He, R., Wang, C., & Tang, X. (2019). Microstructure, Corrosion and Mechanical Properties of TiC Particles/Al-5Mg Composite Fillers for Tungsten Arc Welding of 5083 Aluminum Alloy. *Materials (Basel), 12*(18). doi:10.3390/ma12183029

Jannet, S., Mathews, P. K., & Raja, R. (2014). Comparative investigation of friction stir welding and fusion welding of 6061 T6 – 5083 O aluminum alloy based on mechanical properties and microstructure. *Bulletin of the Polish Academy of Sciences Technical Sciences, 62*(4), 791-795. doi:10.2478/bpasts-2014-0086

Lei, X., Deng, Y., Peng, Y., Yin, Z., & Xu, G. (2013). Microstructure and Properties of TIG/FSW Welded Joints of a New Al-Zn-Mg-Sc-Zr Alloy. *Journal of Materials Engineering and Performance, 22*(9), 2723-2729. doi:10.1007/s11665-013-0577-0

Liu, Y., Wang, W., Xie, J., Sun, S., Wang, L., Qian, Y., . . . Wei, Y. (2012). Microstructure and mechanical properties of aluminum 5083 weldments by gas tungsten arc and gas metal arc welding. *Materials Science and Engineering: A, 549*, 7-13. doi:https://doi.org/10.1016/j.msea.2012.03.108

Maamoun, A. H., Xue, Y. F., Elbestawi, M. A., & Veldhuis, S. C. (2018). Effect of Selective Laser Melting Process Parameters on the Quality of Al Alloy Parts: Powder Characterization, Density, Surface Roughness, and Dimensional Accuracy. *Materials (Basel, Switzerland), 11*(12), 2343. doi:10.3390/ma11122343

Mäkikangas, J., Rautio, T., Mustakangas, A., & Mäntyjärvi, K. (2019). Laser welding of AlSi10Mg aluminium-based alloy produced by Selective Laser Melting (SLM). *Procedia Manufacturing, 36*, 88-94. doi:https://doi.org/10.1016/j.promfg.2019.08.013

Matilainen, V.-P., Pekkarinen, J., & Salminen, A. (2016). Weldability of Additive Manufactured Stainless Steel. *Physics Procedia, 83*, 808-817. doi:10.1016/j.phpro.2016.08.083

Michler, M., Hollmann, P., Zenker, R., & Buchwalder, A. (2021). Investigation of Pore Reduction in Hybrid Joints of Conventionally and Additively Manufactured AlSi10Mg Using Electron Beam Welding. *Advanced Engineering Materials, 23*(6), 2001325. doi:https://doi.org/10.1002/adem.202001325

Olakanmi, E. O., Cochrane, R. F., & Dalgarno, K. W. (2015). A review on selective laser sintering/melting (SLS/SLM) of aluminium alloy powders: Processing, microstructure, and properties. *Progress in Materials Science, 74*, 401-477. doi:https://doi.org/10.1016/j.pmatsci.2015.03.002

Røyset, J., & Ryum, N. (2005). Scandium in aluminum alloys. *International Materials Reviews, 50*, 19-44. doi:10.1179/174328005X14311

Røyset, J., & Ryum, N. (2005). Some comments on the misfit and coherency loss of Al3Sc particles in Al–Sc alloys. *Scripta Materialia, 52*(12), 1275-1279. doi:https://doi.org/10.1016/j.scriptamat.2005.02.023

Santos Junior, M., Machado, A., Falco Sales, W., Barrozo, M., & Ezugwu, E. (2016). Machining of aluminum alloys: a review. *The International Journal of Advanced Manufacturing Technology, 86*. doi:10.1007/s00170-016-8431-9

Schwarz, A., Schleser, M., Gerhards, B., Popoola, P., & Gebhardt, A. (2021). Welding of additive manufactured AlSi10mg: using laser welding in a vacuum for high quality weld seams - a new approach to welding LPBF manufactured AlSi10mg. *South African Journal of Industrial Engineering, 32*. doi:10.7166/32-4-2513

Shanavas, S., & Dhas, J. (2017). *Weldability of AA 5052 H32 aluminium alloy by TIG welding and FSW process: A comparative study.* Paper presented at the IOP Conf. Ser.: Mater. Sci. Eng.

Spierings, A. B., Dawson, K., Heeling, T., Uggowitzer, P. J., Schäublin, R., Palm, F., & Wegener, K. (2017). Microstructural features of Sc- and Zr-modified Al-Mg alloys processed by selective laser melting. *Materials & Design, 115*, 52-63. doi:https://doi.org/10.1016/j.matdes.2016.11.040

Spierings, A. B., Dawson, K., Kern, K., Palm, F., & Wegener, K. (2017). SLM-processed Sc- and Zr- modified Al-Mg alloy: Mechanical properties and microstructural effects of heat treatment. *Materials Science and Engineering: A, 701*, 264-273. doi:10.1016/j.msea.2017.06.089

Spierings, A. B., Dawson, K., Voegtlin, M., Palm, F., & Uggowitzer, P. J. (2016). Microstructure and mechanical properties of as-processed scandium-modified aluminium using selective laser melting. *CIRP Annals, 65*(1), 213-216. doi:10.1016/j.cirp.2016.04.057

Subbaiah, K. (2019, 2019). *Comparative Evaluation TIG and FS Welding of Cast Al–Mg–Sc Alloy.* Paper presented at the Advances in Manufacturing Processes, Singapore.

Wang, B., Chen, X.-h., Pan, F.-s., Mao, J.-j., & Fang,

Y. (2015). Effects of cold rolling and heat treatment on microstructure and mechanical properties of AA 5052 aluminum alloy. *Transactions of Nonferrous Metals Society of China, 25*(8), 2481-2489. doi:https://doi.org/10.1016/S1003-6326(15)63866-3

Weingarten, C., Buchbinder, D., Pirch, N., Meiners, W., Wissenbach, K., & Poprawe, R. (2015). Formation and reduction of hydrogen porosity during selective laser melting of AlSi10Mg. *Journal of Materials Processing Technology, 221*, 112-120. doi:https://doi.org/10.1016/j.jmatprotec.2015.02.013

Wits, W. W., & Becker, J. M. J. (2015). Laser Beam Welding of Titanium Additive Manufactured Parts. *Procedia CIRP, 28*, 70-75. doi:https://doi.org/10.1016/j.procir.2015.04.013

Wong, K. V., & Hernandez, A. (2012). A Review of Additive Manufacturing. *ISRN Mechanical Engineering, 2012*, 1-10. doi:10.5402/2012/208760

Xu, G., Qian, J., Xiao, D., Deng, Y., Lu, L., & Yin, Z. (2016). Mechanical Properties and Microstructure of TIG and FSW Joints of a New Al-Mg-Mn-Sc-Zr Alloy. *Journal of Materials Engineering and Performance, 25*(4), 1249-1256. doi:10.1007/s11665-016-1942-6

Xu, P., Jiang, F., Meng, S., Yi, K., Jiang, J., Cao, Q., & Peng, Y. (2018). Microstructure and Mechanical Properties of Al-Mg-Sc-Zr Alloy Variable Polarity Plasma Arc Welding Joint. *Journal of Materials Engineering and Performance, 27*, 4783. doi:10.1007/s11665-018-3549-6

Ye, Z., Huang, J., Gao, W., Zhang, Y., Cheng, Z., Chen, S., & Yang, J. (2017). Microstructure and mechanical properties of 5052 aluminum alloy/mild steel butt joint achieved by MIG-TIG double-sided arc welding-brazing. *Materials & Design, 123*, 69-79. doi:https://doi.org/10.1016/j.matdes.2017.03.039

Zazi, N., Ifires, M., Mehala, S., & Chopart, J. P. (2017). Corrosion behavior on the different zones of AA2014 welded aluminum alloy by AA5554 filler aluminum alloy with TIG process: Before and after solution heat treatments followed by ageing. *Russian Journal of Non-Ferrous Metals, 58*(5), 516-524. doi:10.3103/s1067821217050169

Zhang, B., Li, Y., & Bai, Q. (2017). Defect Formation Mechanisms in Selective Laser Melting: A Review. *Chinese Journal of Mechanical Engineering, 30*(3), 515-527. doi:10.1007/s10033-017-0121-5